2021-12

How Consistent Are Estimates of Roughness Parameters on a Rough Coral Reef?

Lindhart, M

10.1029/2021jc017825
Journal of Geophysical Research: Oceans
American Geophysical Union (AGU)

JGR Oceans

RESEARCH ARTICLE
10.1029/2021JC017825

How Consistent Are Estimates of Roughness Parameters on a Rough Coral Reef?

M. Lindhart[1], S. G. Monismith[1], A. Khrizman[2], D. Mucciarone[2], and R. Dunbar[2]

[1]Department of Civil and Environmental Engineering, Bob and Norma Street Environmental Fluid Mechanics Laboratory, Stanford University, Stanford, CA, USA, [2]Earth Systems Science, Stanford University, Stanford, CA, USA

Key Points:

- Due to resource limitations, friction velocities and drag coefficients are often based on a single instrument
- Observations show correlation of friction velocities from four velocimeters of varying spatiotemporal resolution deployed on the same reef
- We compare drag coefficients calculated using curve-fitting and photogrammetry, which yield lower correlation due to localized flow features

Supporting Information:

Supporting Information may be found in the online version of this article.

Correspondence to:

M. Lindhart,
lindhart@stanford.edu

Citation:

Lindhart, M., Monismith, S. G., Khrizman, A., Mucciarone, D., & Dunbar, R. (2021). How consistent are estimates of roughness parameters on a rough coral reef? *Journal of Geophysical Research: Oceans*, *126*, e2021JC017825. https://doi.org/10.1029/2021JC017825

Received 24 JUL 2021
Accepted 8 NOV 2021

Abstract Coral reefs are hydrodynamically rough, creating turbulent boundary layers that transport and mix various scalars that impact reef processes and also can be used to monitor reef health. Often reef boundary layer characteristics derived from a single instrument are assumed to accurately represent the study site. This approach relies on two assumptions: first, that the boundary layer is relatively homogeneous across the area of interest, and second, that two instruments displaced in space or with different spatiotemporal resolution would produce similar results when sampling the same flow. We deployed four velocimeters over a 15 × 20 m reef at 10 m depth in the Chagos Archipelago. The site had a 1 m tidal range, and waves were primarily locally generated wind waves with $H_{rms} < 0.5$ m. Depth-averaged currents were typically 0.2 m/s. Friction velocities derived directly from Reynolds stress measurements by fitting the law of the wall show agreement between instruments (pairwise coefficients of determination R^2 ranged from 0.53 to 0.86). Thus, the boundary layer appears to be spatially homogeneous, at least at the scale of our array, and it appears that in the present case friction velocities from one instrument are indeed generally representative of the site. We calculate drag coefficients using curve-fitting and Structure-from-Motion photogrammetry, and while we find general agreement between estimates one instrument in particular produces drag coefficients an order of magnitude larger in comparison. Hence, some variability between instruments was observed, notably when high-resolution instruments measured localized flow features.

Plain Language Summary Coral reefs are characterized by variable bottom features at scales from small coral polyps to rocky substrates and large bommies. This variability is often present on scales of centimeters to tens of meters. However, scientists seldom have enough resources in terms of time and equipment to fully instrument reefs to capture this variability, and often rely on assumptions that their measurements are representative of a larger area while sampling a small subset. One feature of particular interest is the boundary layer, the bottom part of the water column where the current interacts with the corals. Understanding the boundary layer allows scientists to infer a wealth of information, including reef metabolism and input parameters for computer models. In this study, we placed four instruments using different measurement approaches over a 15 × 2 m area of a reef in the Indian Ocean to test whether estimates of the flow were comparable when measured at different locations with different instruments. Estimates agreed overall on the flow characteristics, except from instruments measuring localized flow features close to the corals. Thus, our results offer support to the often implied assumption that we can capture important flow parameters on coral reefs in spite of limited resources.

1. Introduction

Turbulent boundary layers, created by flws interacting with the rough topography of coral reefs, are important to many aspects of reef function and health (Davis et al., 2021). For example, turbulent boundary layers are important to coral health by supporting nutrient uptake (Lowe & Falter, 2015). For an unstratified, turbulent flow over a rough bottom, the boundary layer takes the form of the law-of-the-wall (Pope, 2012):

$$u(z) = \frac{u_*}{\kappa} \ln\left(\frac{z-d}{z_0}\right), \tag{1}$$

where $u(z)$ is the horizontal velocity at height z above the bed, u_* is the friction velocity, z_0 is the roughness height, d is the displacement height, and we adopt the von Kármán constant $\kappa = 0.41$ following Nepf (2011). The friction velocity can also be calculated directly from the Reynolds stresses at the bed

$$u_* = |\overline{u'w'}|_b^{1/2}, \tag{2}$$

where u' and w' are the instantaneous velocity deviations from the mean in the horizontal and vertical direction, respectively, and the bar indicates a time average. Equation 1 has been found to accurately describe boundary layer flow on coral reefs, see e.g., Lentz et al. (2016) and Rosman and Hench (2011). In particular, Reidenbach et al. (2006) found u_* values determined by fitting the law-of-the-wall were consistent with values derived by direct measurement of $\overline{u'w'}$ and from inferred rates of turbulent kinetic energy dissipation on three reef sites near Eilat in the Gulf of Aqaba. Indeed, it is remarkable that despite the complexity of coral surfaces, the log law provides a remarkably good description of the structure of flows over many reefs (Davis et al., 2021). Consequently, the complexity of flows in and among the corals themselves is not considered as the lowest heights of our measurements were well above the corals themselves, a condition that likely describes most velocity measurements made in the field on reefs. These complexities include local wakes and small-scale shear layers that scale with local coral colony size, that is, 10's of cms (Asher & Shavit, 2019).

The friction velocity is important to reef biogeochemistry. In a series of papers, Atkinson and colleagues [see e.g., Falter et al., 2005] showed that nutrient uptake by reefs can be mass-transfer limited such that fluxes to reef communities are directly proportional to u_*. In like fashion, boundary layer velocity measurements can be combined with measurements of concentration gradients of scalars such as oxygen or total alkalinity in order to estimate chemical fluxes and thus to estimate metabolic rates of reefs at time scales as short as minutes (McGillis et al., 2011; Monismith et al., 2010). For example, the Benthic Ecosystem and Acidification Measurement System (BEAMS) method, introduced by Takeshita et al. (2016), is a flux-gradient method based on finding u_* by fitting the law-of-the-wall to observed velocity profile, and then computing the flux using the corresponding eddy diffusivity $\kappa u_* z$. Thus, to generalize these results to a section of a reef scaling with the "footprint" from which the flux is derived (Berg et al., 2007), the measured value of u_* must be assumed to be representative of turbulence at the scale of interest. Typically, the upstream distance of contribution to a flux estimate is given by the footprint (McGillis et al., 2011)

$$L(z) = \frac{\bar{u}z}{u_*} = \frac{\ln(z/z_0)z}{\kappa}. \tag{3}$$

McGillis et al. (2011) and Takeshita et al. (2016) report footprints of 6 and 10 m, respectively.

Bottom drag is often described using the drag coefficient, C_D,

$$C_D = \left(\frac{u_*}{u_{\text{ref}}}\right)^2, \tag{4}$$

where u_{ref} is the reference velocity, typically either the depth-averaged velocity in shallow flows or the velocity at a fixed height, for example, $z = 1$ m above bottom (Lentz et al., 2017). Drag coefficients are widely used in modeling reef flows, where they are used as tuning parameters that are adjusted to best match observed flows [e.g., Lowe et al., 2009]. Recently, efforts have aimed to determine C_D *a priori* based on bottom roughness, z_0 and depth, e.g., Rogers et al. (2018) showed that z_0 could be parameterized in terms of statistics of the bottom topography. Given the wide variety of reef morphologies, the generality of their results remains to be seen.

It is evident that estimates of u_* are essential to studying reef health and hydrodynamics from multiple perspectives. This raises the following question: To what extent are derived values of u_*, z_0, and C_D from a single instrument representative of hydrodynamic behavior of reef flows at larger-scales given the spatial heterogeneity of coral reefs? In order to scale up reef metabolism rates, or use a drag coefficient in a numerical model, the turbulent boundary layer parameterization must be applicable to a larger area of the reef than what is typically feasible to measure. Two assumptions are necessary to extrapolate local measurements to a larger region: (a) The boundary layer and thus the topographic scales that constitute roughness must be relatively homogeneous over the area of interest; (b) The observed boundary layer characteristics should be independent of the instrument; that is, results should not be sensitive to the location or configuration of an instrument. The second assumption, while primarily one of methodology, is nonetheless important since the variety of instruments used to estimate u_* have different capabilities in terms of what they can resolve, from fast measurements of localized turbulence properties to ensemble-averaged measurements of the water column mean flows.

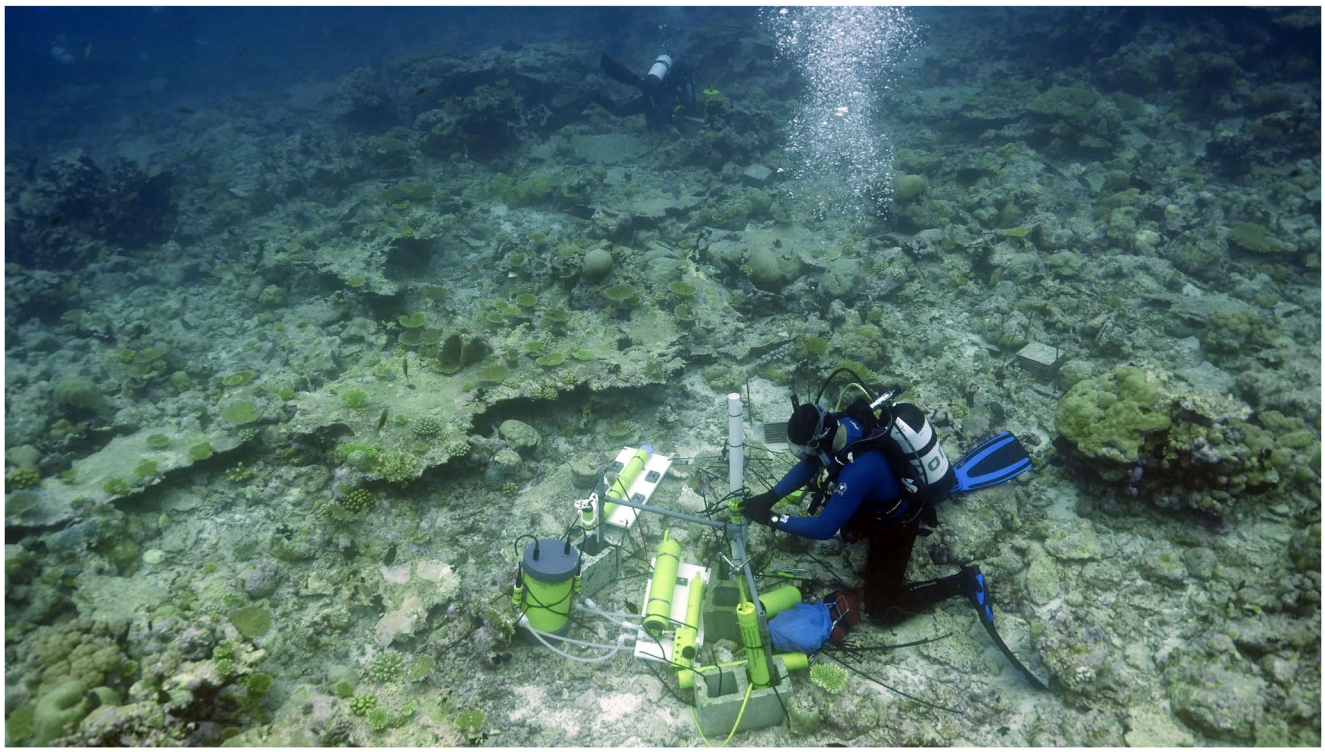

Figure 1. Photo of the reef, taken on March 19, 2019 during deployment. In front, multiple instruments are being deployed, including the ADV and ADP. The Signature is being deployed at the top of the photo toward the back. The photo is taken looking approximately north.

This paper presents results from a 2-week deployment made on a reef in the Chagos Archipelago in March 2019, where, along with the deployment of biogeochemical instruments designed to quantify reef chemistry, four different velocimeters were deployed in a 15 × 20 m area. A photo of the reef is found in Figure 1, and a high-resolution orthomosaic is in Text S1 in Supporting Information S1. Using two techniques, log-fits to mean velocity profiles and calculation of Reynolds stresses, we computed time series of u_* for each instrument. We use Structure-from-Motion (SfM) (Ullman, 1979) to create a scaled digital elevation model (DEM = bathymetry) of the reef to quantify the physical roughness heights of the reef and their spatial variability. We find a reasonable correlation between all estimates of the friction velocity u_* (R^2 ranging from 0.53 to 0.86), implying that all four instruments sampled a similar, larger scale flow structure, and estimates from any one of the instrument were representative of u_* in the 15 × 20 m area studied. Photogrammetry-derived drag coefficients showed agreement with those derived from instruments observing large-scale flow features; however, this is not the case when comparing to an instrument capable of resolving highly localized flow features. We show that while computed roughness parameters are in general agreement, care should be taken when comparing instruments of widely different spatiotemporal resolutions and measuring volumes.

2. Field Site and Methods

As part of a larger initiative to study the British Indian Ocean Territory Marine Protected Area (Hays et al., 2020), measurements were made on the fringing reef off Île Anglaise (lat: −5.3387°, lon: 72.2133°) between March 10 to March 24, 2019. Île Anglaise is part of Salomon atoll in the Chagos Archipelago [Figure 2a]. A list of the deployed velocimeters is given in Table 1, which also lists sampling rates and associated deployment parameters. Instrument locations are shown in Figure 2. To sample different parts of the water column at different spatiotemporal resolutions, we deployed four velocimeters: (a) an RDI Acoustic Doppler Current Profiler (ADCP) with a measurement range of 10 m at a 0.25 -m resolution, (b) a Nortek Signature ADCP with a range of 13 m at a 0.5 m resolution, (c) a Nortek Acoustic Doppler Profiler (ADP) with a 1.86 -m range at a 3 -cm resolution, and (d) a Nortek Acoustic Doppler Velocimeter that measured single-point velocities at a about 1 m above the canopy.

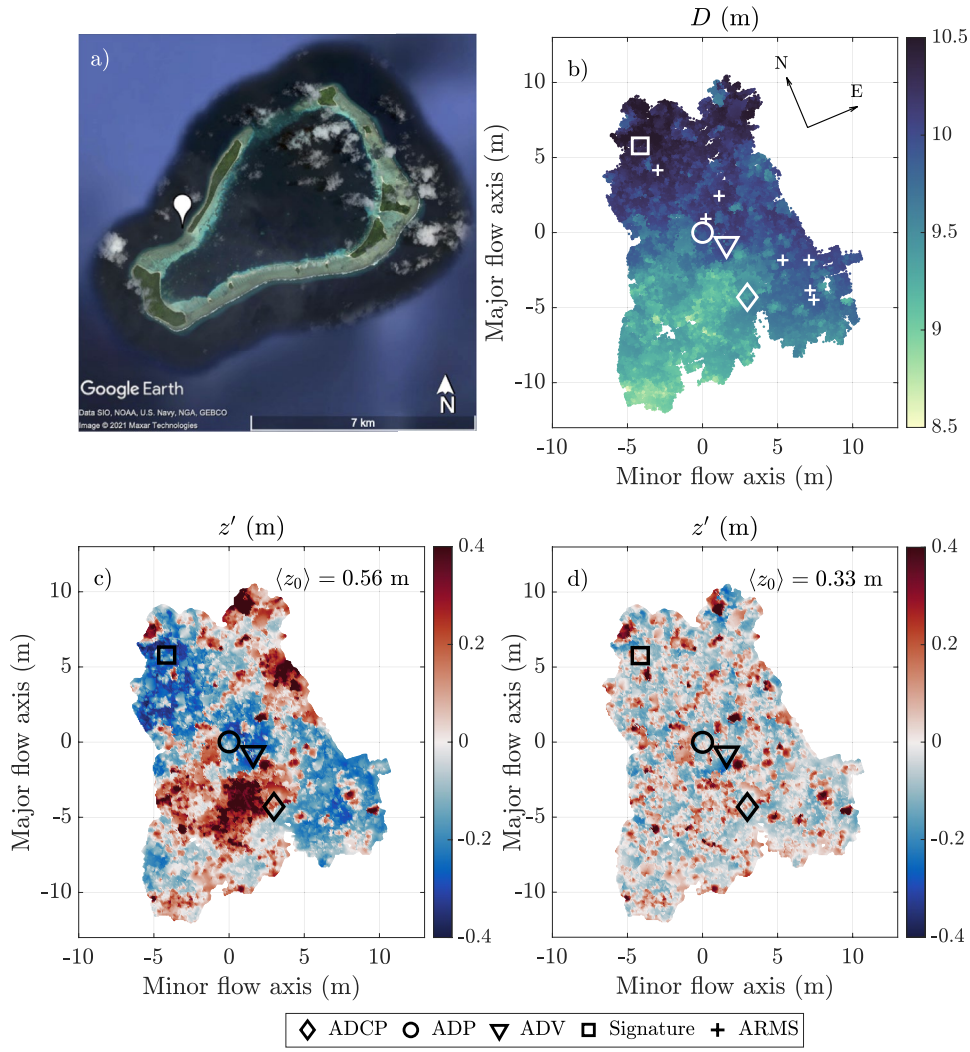

Figure 2. Origin at latitude −5.3387° and longitude 72.2133° (a) Salomon Atoll, Chagos. The field site is just west of Île Anglaise island. Map data: Google Earth, CNES/Airbus. (b) Bathymetry of the site derived from Structure-from-Motion. Symbols indicate locations of instruments and ARMS collectors. (c) Bathymetry (DEM), linearly detrended in x and y. (d) Bathymetry, detrended with a 2 × 2 m moving average filter. Values of $\langle z_0 \rangle$ are calculated using Equation 5.

A high-resolution 3D model of the reef showing the benthos and community structure in detail is available in the data repository associated with this paper.

The site had a mean depth of 10 m and an approximate 1 m tidal range. The two-week deployment captured a spring-neap cycle. Observed waves were primarily locally generated wind waves with root-mean-square wave heights less than 0.5 m and periods around 2–5 s. Depth-averaged currents were typically 0.2 m/s, with a maximum of 0.8 m/s. The principal flow direction was along-shore, see major flow axis in Figure 2.

Depending on the instrument, we use two different methods to estimate u_*. Equation 1 was fit to velocity profiles measured by the ADP, ADCP, and Signature to estimate u_* and z_0 (Table 1, last column). Initially, velocity profiles were fit to include the displacement height d in Equation 1; however, we found that median estimates of d were approximately 0 m, and setting $d = 0$ made no discernible effect on computed values of u_* and z_0. The vertical extent of the profiles ranged from approximately 1–4 m, depending on the vertical resolution of the instrument, see Figure 3. The ADP had the highest vertical resolution of 3 cm [Figure 3a], whereas the Signature ADP the lowest resolution of 0.5 m [Figure 3c]. Only profiles for which the coefficient of determination $R^2 \geq 0.8$ were used in the results shown throughout.

Table 1
Instruments Deployed, and Methods Used to Calculate u_* and z_0

Instrument	Sampling	Resolution	Depth (m)	u_* and z_0 calculation
2 MHz Nortek ADP HR	512 profiles at 1 Hz every 30 min	62 bins of 3 cm, blanking distance 0.43 m	10	Log-fit $u(z) = u_*/\kappa \cdot \ln(z/z_0)$[a], of lower 22 bins, 512 profiles at 1 Hz.
1200 kHz RDI ADCP	Continuous, 5 min ensembles	40 bins of 25 cm, blanking distance 0.38 m	9.3	Log-fit $u(z) = u_*/\kappa \cdot \ln(z/z_0)$[a], of lower bins 2 to 9, 5 min ensembles averages.
Nortek **ADV**	8192 profiles at 16 Hz every 30 min	Volume 14.9 mm	10	$u_* = \lvert\overline{u'w'}\rvert^{1/2}$ of 8192 samples at 16 Hz, no z_0.
Nortek Signature 1,000 ADCP	Continuous, profiling at 2 Hz	27 bins of 0.5 m blanking distance 0.6 m	10.7	Log-fit $u(z) = u_*/\kappa \cdot \ln(z/z_0)$[a], of lower 8 bins[b], 600 profiles, 2 Hz.

Note. All instruments were bottom-mounted and upward-facing.
[a]We first estimated the logarithmic fits with three fitting parameters: u_*, z_0 and d. However, $d = 0$ in all but a few instances. Therefore, we set $d = 0$, and analyzed our data with two fitting parameters: u_* and z_0. [b]About halfway through the deployment, the Signature 1,000 shifted on the substrate, and a coral canopy obscured bins in the range 2.6–3.6 m. The two bins in question were not included in the log fits.

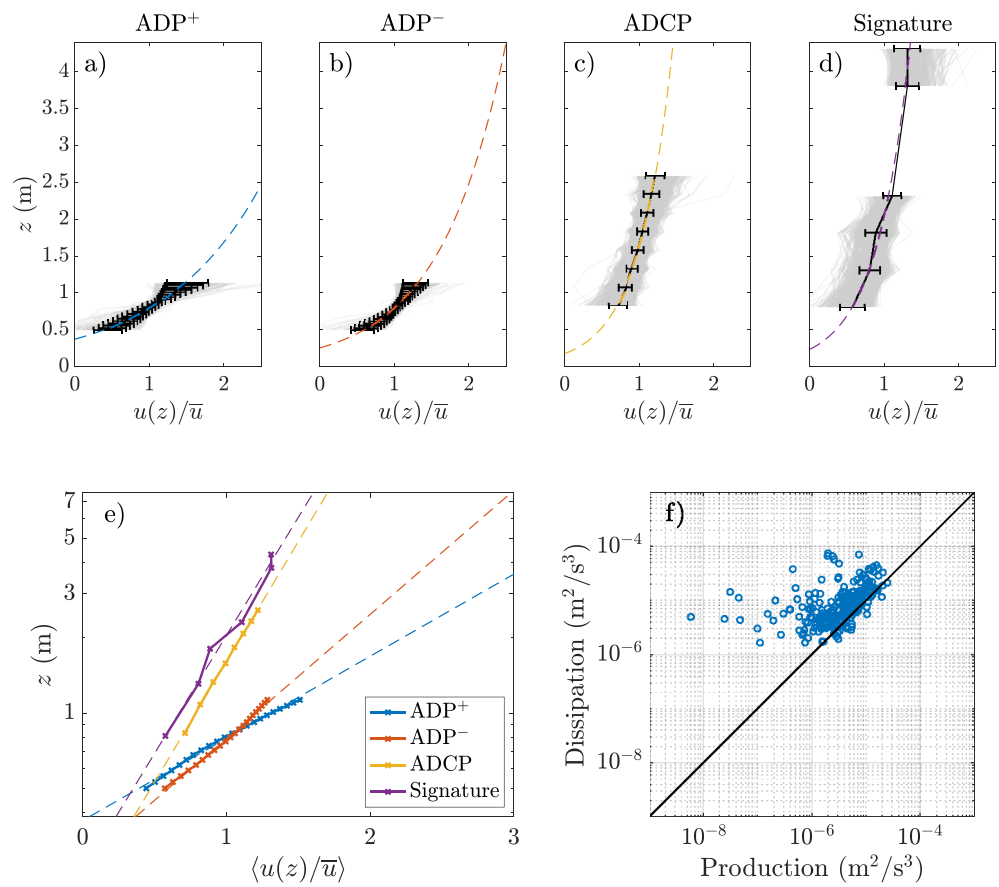

Figure 3. (a)–(d) In gray, velocity profiles of $u(z)$ normalized by the mean velocity $\bar{u}$ for all profiles where $R^2 \geq 0.8$ are shown. The black error bars show the time-averaged value and one standard deviation of each vertical bin. The dashed lines are the log profiles based on a best fit of the time-averaged profiles. Figures (a) and (b) show the ADP profiles when flow is directed north and south, respectively. (e) Time-averaged profiles and best fit as in (a)–(d), here on a logarithmic scale. (f) Dissipation of TKE as derived from the ADV and production of TKE as derived from the ADV and ADP.

From the ADV, we calculated Reynolds stresses for each 8.5 min burst. Although the site experienced limited wave forcing, we first separated wave and turbulent stresses following Benilov and Filyushkin (1970) and calculated u_* from the turbulent stresses using Equation 2. We did not calculate z_0 from the ADV data. For the ADP, ADCP, and Signature, we calculated the drag coefficient using Equation 4 and a reference velocity $u_{\text{ref}} = u(1\text{ m})$.

For development of a SfM bathymetric model, 476 photos were collected using a Panasonic GH4 camera in a Nauticam GH4 underwater housing with a 7-inch dome port. The camera diver swam slowly about 1.5 m above the seabed following a grid like pattern over an area of 15 × 20 m with the BEAMS experiment at the center, aiming to achieve 50% overlap in fields of image capture. After filtering out photos containing non-target objects or with non-vertical camera orientations, 390 photos were used for modeling. Fish were masked out of the images manually, and SfM processing was accomplished using Agisoft Metashape Pro following the general protocols, module sequence, and settings (Bayley & Mogg, 2020). Scaling was established using 19 X/Y (horizontal) control points from the Autonomous Reef Monitoring Structures (ARMS) instruments deployed through the study area [each ARMS plate is 22.5 × 22.5 cm, see locations in Figure 2b]. Depth measurements used to check model-produced bathymetry were made by comparing the DEM depth to observed instrument mean depths. The DEM has dimensions of 24,367 × 27,474 with a real-world pixel dimension of 1.1 mm. Estimate average positional error is up to 3.2 mm.

The SfM data were used to compare the drag coefficients derived from hydrodynamic observations to the method proposed in Rogers et al. (2018), in which the drag coefficient is derived from topography only. The prospect of estimating drag coefficients without direct velocity measurements is enticing, in particular in its application to numerical models; however, the generality of the method requires validation against field studies. The SfM data were processed according to Rogers et al. (2018) to calculate topographic roughness, $(z')_{\text{rms}}$, and small-scale slope, $\left(\frac{dz'}{d\mathbf{x}}\right)_{\text{rms}}$, to estimate z_0. The reef in Rogers et al. (2018) was on a flat, sandy bed, which served as a vertical datum. Here, the entire reef slopes, obfuscating the distinction between topography and roughness elements. To calculate the topographic roughness heights, we used two methods; (1) fitting a plane to the reef and subtracting the vertical plane coordinate from the bathymetry, essentially detrending the SfM linearly, and (2) creating a 2D moving average filter of 2 × 2 m extent and subtracting the averaged surface from SfM data [Figures 2c and 2d]. For both methods, once the bathymetry is detrended, we follow Rogers et al. (2018) to calculate

$$\langle z_0 \rangle = \frac{4}{\pi}(z')_{\text{rms}} \left(\frac{dz'}{d\mathbf{x}}\right)_{\text{rms}}, \tag{5}$$

where z' is the deviation from the bottom surface shown in Figures 2c and 2d, and $(f)_{\text{rms}} = \langle f^2 \rangle^{1/2}$ is the root-mean-square of the spatially distributed parameter f. The multi-scale roughness of the reef makes the averaging challenging: While local streamwise slope $\frac{dz'}{d\mathbf{x}}$ is easily calculable, both $(z)_{\text{rms}}$ and $\left(\frac{dz'}{d\mathbf{x}}\right)_{\text{rms}}$ depend on the length scale that is assumed to characterize the overall bathymetry variation. The smaller this averaging scale is made, the smaller value of $(z)_{\text{rms}}$ and $\left(\frac{dz'}{d\mathbf{x}}\right)_{\text{rms}}$ that one finds. Further exploration of this issue using SfM data from the Île Anglaise site and other Chagos reef sites will be given elsewhere. Rogers et al. (2018) estimate the drag coefficient by

$$\langle C_D \rangle = \kappa^2 \left[\ln\left(\frac{\langle D \rangle}{\langle z_0 \rangle}\right) + (\Pi - 1)\right]^{-2}, \tag{6}$$

where $\langle D \rangle$ is the mean depth, $\Pi \approx 0.2$ for high Reynolds numbers (Lentz et al., 2017), and $\langle C_D \rangle$ relates the bed shear stress to the depth-averaged velocity. In this work, we estimate drag coefficients for the site using Equation 6 and 4 and compare them below.

3. Results

Figures 3a–3d shows velocity profiles for each sampling period ($u(z)$), normalized by the depth-averaged velocity of the profile ($\bar{u}$). The black lines and error bars show the mean and standard deviation over the entire deployment, and the dashed line shows a logarithmic fit to the time-averaged mean. The fitted profiles outline the boundary layer as observed by each instrument and which part of the profile the instruments are capturing. Similarly, in Figure 3e, the time-averaged profiles and fits are shown on a logarithmic scale, illustrating the linear behavior expected of a velocity profile according to Equation 1.

The development of the logarithmic boundary layer profile relies on a balance between production and dissipation of turbulent kinetic energy (TKE), $P = \epsilon$. Thus, as a check on the validity of applying the log law to the flow and thereby deriving u_*, we estimate production and dissipation separately and compare the two. Production and dissipation are estimated following, for example, Reidenbach et al. (2006). Production is calculated as,

$$P = -\overline{u'w'}\frac{\partial \overline{u}}{\partial z} - \overline{v'w'}\frac{\partial \overline{v}}{\partial z},$$

where the Reynolds stresses are estimated from the ADV and the velocity shear is estimated from the ADP at the same height. We compare to the dissipation, ϵ, calculated according to Shaw et al. (2001),

$$S_{ww}(k) = \frac{9}{55}\left(\frac{4-\cos^2\theta}{3}\right)\alpha\epsilon^{2/3}k^{-5/3}, \tag{7}$$

where S_{ww} is the vertical velocity spectrum, θ is the angle to the mean flow ($\theta = 90°$), $\alpha = 1.56$ is an empirical constant, and the wavenumber k is related to the frequency through Taylor's frozen turbulence hypothesis $f = \frac{\bar{u}k}{2\pi}$. A straight line is fit to the inertial subrange of $\ln(S_{ww})$ as a function of $\ln(f)$, where $S_{ww} \propto f^{-5/3}$. Using a value pair (k_1, $S_{ww}(k_1)$) from the linear fit, ϵ is evaluated through Equation 7. These estimates are found in Figure 3f and show a production-dissipation balance of TKE required for the development of the logarithmic boundary layer and derivation of u_*.

Calculated friction velocities from the four instruments are all similar in magnitude and follow similar trends in Figure 4. The sign of u_* indicates direction as aligned with the major flow axis (Figure 2). Figure 4, top, is an example of friction velocities calculated for a duration of one day.

The five scatter plots in Figure 4 show pairwise comparisons of values of u_* derived from the four velocity time series. Pairwise coefficients of determination R^2 range from 0.53 for the ADP and the ADV up to 0.86 for the Signature and the ADCP. Furthermore, we estimate roughness heights z_0, see Table 2. Mean z_0 values vary between $0.22 - 0.33$ m. Compare this to the physical roughness in Figures 2c and 2d, where roughness elements vary from $|z'| \sim 0 - 0.5$ m, depending on the choice of detrending. Estimates of C_D are found in Table 2, calculated from Equation 4. The calculations distinguish between flow directions.

Figure 5a combines two representative mean ADP profiles, one for northward flow and one for southward flow, both shown on SfM-derived bathymetry. When the flow is directed southward, and approaches the ADP from a relatively flat and deeper area, a well defined law-of-the-wall boundary layer develops. As the flow reverses, it approaches the ADP from the shallower region with larger roughness elements that lies to the south. The velocity profile in this case is typical of a mixed boundary layer either immersed in, or located downstream of, a dense canopy (Chung et al., 2021; Nepf, 2011). While this mixed-layer profile requires the inclusion of the displacement height d in Equation 1 (Rosman & Hench, 2011), the median values of d from fits were close to zero; hence, we set $d = 0$ m throughout. Most importantly, by visualizing topographic and roughness variations at scales ranging from single coral heads to the entire area imaged, and given the position in that area of any velocity sensors, SfM-derived bathymetric data can be used to understand why flow structure might vary with flow direction (Figure 5 and Movie S1 in Supporting Information S1).

4. Discussion

Friction velocities estimated from the four velocity instruments show agreement over the two-week deployment period (Figure 4, R^2 ranging from 0.53 to 0.86). The ADCP and Signature were best correlated, despite being located the farthest apart of all the instrument pairs, likely due to the fact that the two instruments measure at larger spatial scales and thus localized flow features were averaged out in both time and space. This is corroborated by Figure 5b, which shows the two instruments measured almost identical velocity profiles. In contrast, the ADP and ADV sampled the flow closer to the bed at higher resolutions and thus were more likely to be affected by local topography and flow features.

The mean hydrodynamic roughness heights z_0 varied between 0.23 and 0.40 m, with large scatter in particular in the ADCP and Signature estimates (Table 2). These values are comparable to the physical roughness scales in Figure 2. In Figure 2c, just south of the ADP, a large coral canopy protrudes. This is likely the source of the mixed-layer velocity profile observed during northward flow, and the reason the ADP-derived roughness heights

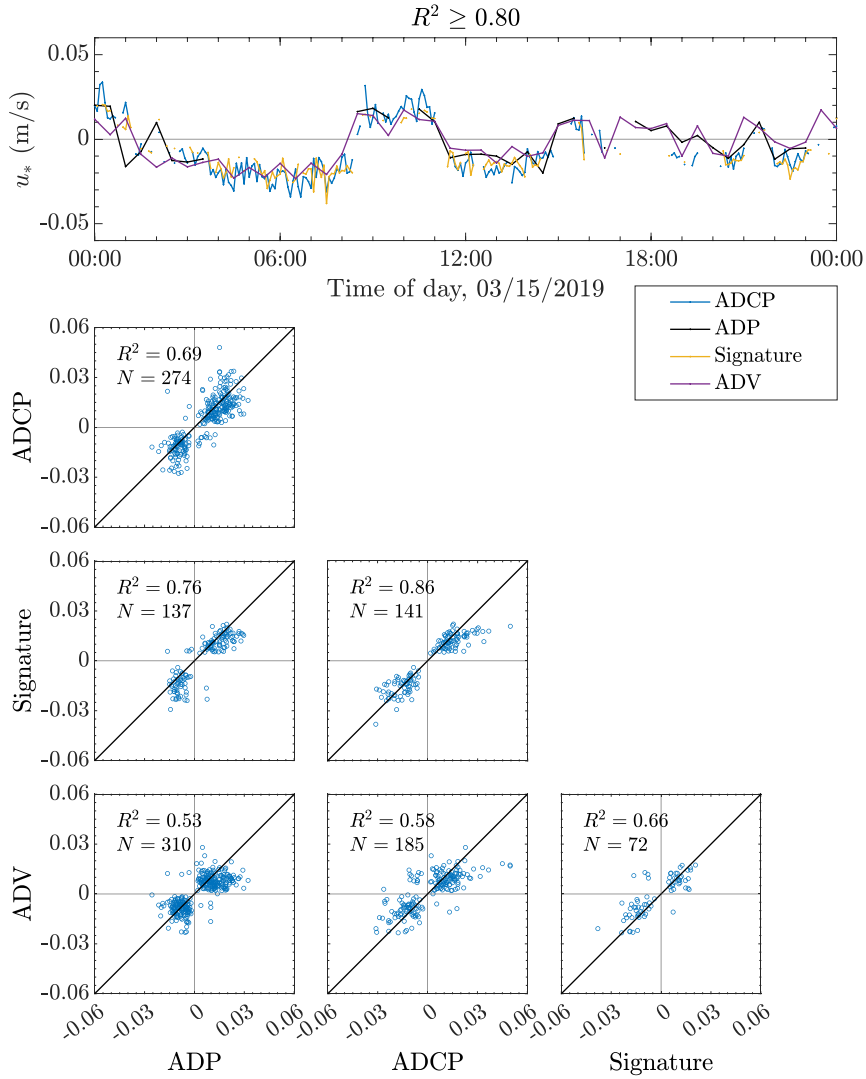

Figure 4. Top: time series example of $u_*(t)$ for all four instruments. For the ADCP, ADP, and Signature: only instances when log fits $R^2 \geq 0.8$ are shown. Bottom: Scatter plots of u_* calculated from each instrument with units m/s. R^2 in upper-left corners are the coefficients of determination between the instruments and N the number of instances used. Positive friction velocities are directed in the positive direction of the major flow axis in Figure 2.

Table 2
Estimated Roughness Parameters

	Logarithmic fits			Equation 5	Equation 4, $u_{ref} = u(1\text{ m})$		Equation 6
	$R^2 \geq 0.8$	z_0^{North} (m)	z_0^{South} (m)	$\langle z_0 \rangle$[a](m)	C_D^{North}	C_D^{South}	$\langle C_D \rangle$[a]
ADCP	56%	0.27 ± 0.22	0.28 ± 0.24		0.05 ± 0.002	0.03 ± 0.001	
ADP	84%	0.34 ± 0.12	0.23 ± 0.13		0.14 ± 0.004	0.05 ± 0.003	
Signature	40%	0.31 ± 0.25	0.40 ± 0.26		0.04 ± 0.002	0.06 ± 0.003	
Linear detrend				0.56			0.04
Moving average detrend				0.33			0.02

Note. Results are given with one standard deviation error.
[a]Following Rogers et al. (2018).

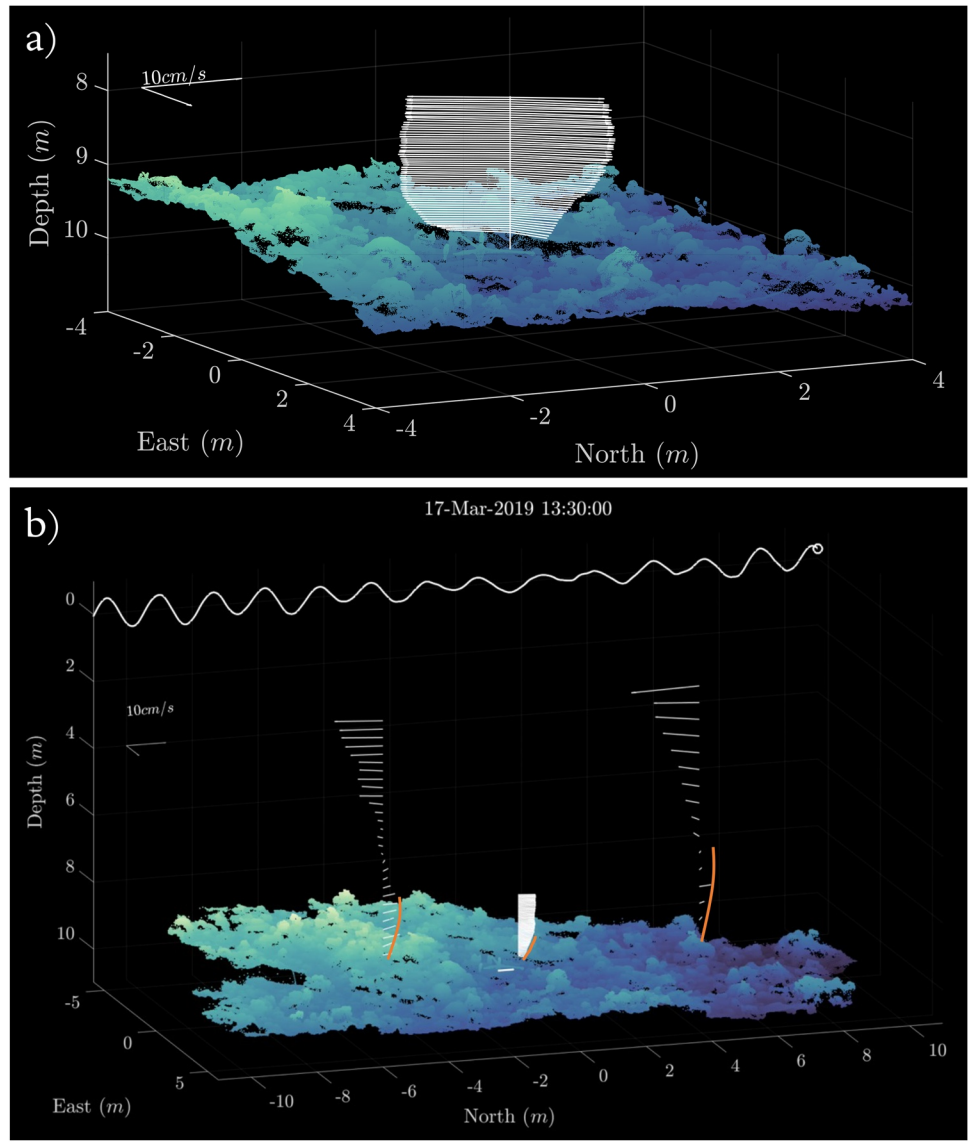

Figure 5. Origin at latitude −5.3387°, and longitude 72.2133°. (a) Quiver plot of ADP velocities superimposed on the DEM from SfM. Northward flow: 11 a.m., March 13, 2019. Southward flow: 1.30 a.m., March 11, 2019. Each quiver plot is the average of 512 profiles at 1 Hz. (b) Mean velocities for a half-hour period, from left to right: ADCP, ADV, ADP, Signature. See full Movie S1 in Supporting Information S1. The orange line indicates the approximate extent over which the curve fitting was done. The white line at zero depth indicates the tidal water level, and the marker indicates the water level at the given time in the video. These figures in Supporting Information S1 were produced using Matlab's Computer Vision Toolbox.

were larger for flows going north than for flows going south (Figures 5a and Table 2). The asymmetry in z_0 suggests that the roughness elements south of the ADP were larger than ones to the north of the ADP, and therefore, the drag for flows from the south was larger as well. In contrast, the flow measured by the ADCP had no significant directional asymmetry, in accordance with Figure 2, since the surrounding surface elements are uniformly small. Unfortunately, data from the Signature have a significant amount of scatter due to large vertical bins and a shift in pitch that required bins 5 and 6 from the bottom to be discarded due to a coral obstructing the beams. It is not possible to say from the z_0 values in Table 2 whether the Signature measured directional asymmetry due to the large uncertainty.

Both Rosman and Hench (2011) and Lentz et al. (2017) reported coral reef drag coefficients that span two orders of magnitude, i.e., from 0.003 to 0.1, with the lower limit being characteristic of canonical, nearly smooth bottoms and the upper limit representing the area-averaged effects of large coral bommies (Hench et al., 2008).

For the ADCP and the Signature, $C_D \simeq 0.03$–0.06, values that are well within values reported for other reefs. The ADP produced direction-dependent drag coefficients in comparison, $C_D = 0.05$ for flows going south, and $C_D = 0.14$ for flows going north, nearly five times larger than the ADCP. We discuss this disparity in Section 4.2.

4.1. Resolving the Boundary Layer

Consistency of the estimated roughness parameters u_* and z_0 shows that the results are largely independent of the instrument configuration and location, suggesting that the boundary layer at this site is approximately spatially homogeneous. The spatial coherence of the mean flow is easily seen in the observed velocity profiles when they are viewed superposed on the reef bathymetry, as in Figure 5 and also shown in the supplementary materials. The ADCP and the Signature recorded similar velocity profiles at a similar spatial resolution, including at times the appearance of a flow reversal approximately halfway through the water column. Thus, friction velocities derived from the two instruments are also similar (as seen in Figure 4). This consistency explains why the u_* correlation is highest between the ADCP and the Signature (Figure 4), in spite of the two instruments being the farthest apart of the four instruments.

While the roughness parameters were largely correlated, some variability between instruments was evident, in particular when bed stress estimation was done using near-bed measurements. The ADV and the ADP derived values u_* were most weakly correlated despite of being closely located, reflecting the fact that they were sampling much more localized, and hence variable flows. For example, the canopy flow velocity profile observed by the ADP was not resolved by either the ADCP or the Signature, where the larger bin sizes tend to average out these effects.

Qualitatively, the differences between what the ADP recorded versus what the ADCP and Signature measured reflects the fact that the area of the bed affecting the flow structure increases with height (Bou-Zeid et al., 2004; Davis et al., 2021), as suggested also by the footprint calculation, Equation 3, which provide estimates of ca. 2 m for the ADP and ca. 10 m for the Signature and the ADP. These simple estimates should be viewed as somewhat approximate as the LES calculations presented in Bou-Zeid et al. (2004); Bou-Zeid et al. (2007) make clear that the physics of flow over spatially varying roughness involve the blending of different turbulence structures with height in a way that depends on the sizes and heights of the individual roughness patches. Practically, it may be the case that despite the extra resolution gained by the use of the high resolution profiling capability of the ADP, using the instrument in this mode made be less useful for determining u_* due to the limited range necessitated by the pulse to pulse coherent processing mode needed to obtain the higher resolution profiles.

4.2. Drag Coefficient Inconsistencies

Estimates of drag coefficients are more varied than those of friction velocities, as seen when comparing the ADP to the ADCP and Signature (Table 2). Friction velocities calculated by fitting a logarithmic boundary layer profile (Equation 1) rely on the overall velocity profile shape and are less sensitive to velocity fluctuations in individual vertical bins. The overall horizontal velocity profile is similar for all instruments (Figure 5) as they are sampling the same large-scale boundary layer flow. The resulting u_* values reflect this homogeneity, which is encouraging since, for example, gradient flux measurements on reefs such as mentioned in Section 2 rely on this assumption. Since calculated fluxes are proportional to u_* a strong bias depending on instrument type or displacement would question the extent to which the result are representative of the reef. In contrast, calculating the drag coefficient by Equation 4 introduces uncertainty associated with the choice of reference velocity. Using $u_{\mathrm{ref}} = 1$ m is a common choice, and as such provides a useful basis for comparing drag coefficients across instruments, reefs, and studies, however, defining the $z = 1$ m on a reef is nontrivial. Reef surface variance is often in the order of 0.1–1 m, and vertical scales of instruments and deployment setups are of order 0.1 m. If $C_D = \left(\frac{u_*}{u_{\mathrm{ref}}}\right)^2$, then underestimating the reference velocity by half overestimates the drag coefficient by a factor of four. Hence, even when two instruments produce comparable friction velocities, the resulting drag coefficients may vary depending on the definition of the reference velocity.

Thus, the question is raised: If only one instrument is available and no comparison can be made between instruments, which metric can be used to gauge the estimated drag coefficient? In this study, we found that using the method outlined by Rogers et al. (2018) produced drag coefficients that were consistent with the ADCP and the

Signature. More studies are needed to examine the generality of the method, especially as it applies to multiscale roughness as outlined in Section 2. The benefit of this method is that it relies exclusively on the geometric characteristics of the reef from SfM, and it takes no more than one or two dives on a site to gather enough images for the generation of a DEM. Pending exploration of the robustness of the method, SfM-derived drag coefficient can serve as a comparison when only one instrument is available.

5. Conclusion

In this paper, we estimated friction velocities from four different instruments with different sampling characteristics, all deployed on the same section of reef. This data allowed us to examine the common (implied) assumptions made in measuring reef bed stresses that the turbulent boundary layer over the reef of interest is relatively homogeneous, and thus that bed stresses derived from an instrument sampling at a single location can be applied to a larger area of interest. Arguably this is made necessary by very practical reasons: such measurements must be made with limited time and resources and instruments locations are often chosen based on by where they can be anchored and nested between corals and rock formations.

In the present case, the comparison of estimates made using four instruments shows significant agreement in friction velocities, with coefficients of determination R^2 ranging from 0.53 to 0.86. This indicates that in spite of differences in instrument characteristics, the presence of large roughness elements, and meter scale heterogeneity in bathymetry, the boundary layer flow at larger scales is be sufficiently homogeneous to be described by the law-of-the-wall, and thus can be characterized by any instrument that resolves the flow over heights far enough from the boundary to not be strongly affected by local roughness elements. In comparison, drag coefficients showed larger variability between estimates based on the choice of reference velocity in the calculations. Overall, our Île Anglaise observations show that limited hydrodynamic measurements can usefully support larger interdisciplinary studies quantifying reef processes.

Finally, from the standpoint of understanding coral reef hydrodynamics, further work clarifying how flows over complex, spatially variable roughness combine to produce log layers seems warranted. As a starting point, more detailed near-bed measurements, like those of Hench and Rosman (2013) would be valuable, especially if they could be interpreted in the light of the blending height model of (e.g.,) Bou-Zeid et al. (2007). In this regard, SfM could provide the detailed topography measurements required to define the roughness. Then what would be needed is the complementary $\mathcal{O}$(m) scale velocity measurements, made using a whole field measurement technique such as Particle Tracking Velocimetry.

Data Availability Statement

The data used in this study can be accessed online at https://purl.stanford.edu/hk123fd9747.

Acknowledgments
M. Lindhart gratefully acknowledges the support of the Stanford Graduate Fellowship and the Gerald J. Lierberman Fellowship. This work was supported by a grant from the Bertarelli Program in the Marine Sciences, and National Science Foundation grant OCE-1948189. We are grateful to the captain and crew of the support vessel and Dakota Riemersma for assistance with photogrammetry processing. The authors also thank Andrew Pomeroy and an anonymous reviewer whose comments helped improve this manuscript.

References

Asher, S., & Shavit, U. (2019). The effect of water depth and internal geometry on the turbulent flow inside a coral reef. *Journal of Geophysical Research: Oceans*, *6124*(6), 3508–3522. https://doi.org/10.1029/2018jc014331

Bayley, D. T., & Mogg, A. O. (2020). A protocol for the large-scale analysis of reefs using structure from motion photogrammetry. *Methods in Ecology and Evolution*, *11*(11), 1410–1420. https://doi.org/10.1111/2041-210X.13476

Benilov, A. Y., & Filyushkin, B. N. (1970). Applications of the linear filtration methods to the fluctuation analysis in the sea upper layer. *Izvestiya - Atmospheric and Oceanic Physics*, *6*, 810–819.

Berg, P., Røy, H., & Wiberg, P. L. (2007). Eddy correlation flux measurements: The sediment surface area that contributes to the flux. *Limnology & Oceanography*, *52*(4), 1672–1684. https://doi.org/10.4319/lo.2007.52.4.1672

Bou-Zeid, E., Meneveau, C., & Parlange, M. B. (2004). Large-eddy simulation of neutral atmospheric boundary layer flow over heterogeneous surfaces: Blending height and effective surface roughness. *Water Resources Research*, *40*(2), 1–18. https://doi.org/10.1029/2003WR002475

Bou-Zeid, E., Parlange, M. B., & Meneveau, C. (2007). On the parameterization of surface roughness at regional scales. *Journal of the Atmospheric Sciences*, *64*(1), 216–227. https://doi.org/10.1175/jas3826.1

Chung, H., Mandel, T., Zarama, F., & Koseff, J. R. (2021). Local and nonlocal impacts of gaps on submerged canopy flow. *Water Resources Research*, *257*(2), 1–20. https://doi.org/10.1029/2019wr026915

Davis, K. A., Pawlak, G., & Monismith, S. G. (2021). Turbulence and coral reefs. *Annual Review of Marine Science*, *113*(1), 042120071823. https://doi.org/10.1146/annurev-marine-042120-071823

Falter, J. L., Atkinson, M. J., & Coimbra, C. F. (2005). Effects of surface roughness and oscillatory flow on the dissolution of plaster forms: Evidence for nutrient mass transfer to coral reef communities. *Limnology & Oceanography*, *50*(1), 246–254. https://doi.org/10.4319/lo.2005.50.1.0246

Hays, G. C., Koldewey, H. J., Andrzejaczek, S., Attrill, M. J., Barley, S., Bayley, D. T. I., et al. (2020). A review of a decade of lessons from one of the world's largest MPAs: Conservation gains and key challenges. *Marine Biology*, *167*(11), 159. https://doi.org/10.1007/s00227-020-03776-w

Hench, J. L., Leichter, J. J., & Monismith, S. G. (2008). Episodic circulation and exchange in a wave-driven coral reef and lagoon system. *Limnology & Oceanography*, *53*(6), 2681–2694. https://doi.org/10.4319/lo.2008.53.6.2681

Hench, J. L., & Rosman, J. H. (2013). Observations of spatial flow patterns at the coral colony scale on a shallow reef flat. *Journal of Geophysical Research: Oceans*, *118*(3), 1142–1156. https://doi.org/10.1002/jgrc.20105

Lentz, S. J., Churchill, J. H., Davis, K. A., Farrar, J. T., Pineda, J., & Starczak, V. (2016). The characteristics and dynamics of wave-driven flow across a platform coral reef in the Red Sea. *Journal of Geophysical Research: Oceans*, *2121*(2), 1360–1376. https://doi.org/10.1002/2015jc011141

Lentz, S. J., Davis, K. A., Churchill, J. H., & DeCarlo, T. M. (2017). Coral reef drag coefficients – water depth dependence. *Journal of Physical Oceanography*, *47*(5), 1061–1075. https://doi.org/10.1175/jpo-d-16-0248.1

Lowe, R. J., & Falter, J. L. (2015). Oceanic forcing of coral reefs. *Annual Review of Marine Science*, *7*(January 2015), 43–66. https://doi.org/10.1146/annurev-marine-010814-015834

Lowe, R. J., Falter, J. L., Monismith, S. G., & Atkinson, M. J. (2009). A numerical study of circulation in a coastal reef-lagoon system. *Journal of Geophysical Research: Oceans*, *114*(6), 873–893. https://doi.org/10.1029/2008JC005081

McGillis, W. R., Langdon, C., Loose, B., Yates, K. K., & Corredor, J. (2011). Productivity of a coral reef using boundary layer and enclosure methods. *Geophysical Research Letters*, *38*(3). https://doi.org/10.1029/2010gl046179

Monismith, S. G., Davis, K. A., Shellenbarger, G. G., Hench, J. L., Nidzieko, N. J., Santoro, A. E., & Genin, A. (2010). Flow effects on benthic grazing on phytoplankton by a Caribbean reef. *Limnology & Oceanography*, *55*(5), 1881–1892. https://doi.org/10.4319/lo.2010.55.5.1881

Nepf, H. M. (2011). Flow and transport in regions with aquatic vegetation. *Annual Review of Fluid Mechanics*, *44*, 123–142. https://doi.org/10.1146/annurev-fluid-120710-101048

Pope, S. B. (2012). The equations of fluid motion. *Turbulent Flows*, 10–33. https://doi.org/10.1017/cbo9780511840531.004

Reidenbach, M. A., Monismith, S. G., Koseff, J. R., Yahel, G., & Genin, A. (2006). Boundary layer turbulence and flow structure over a fringing coral reef. *Limnology & Oceanography*, *51*(5), 1956–1968. https://doi.org/10.4319/lo.2006.51.5.1956

Rogers, J. S., Maticka, S. A., Chirayath, V., Woodson, C. B., Alonso, J. J., & Monismith, S. G. (2018). Connecting flow over complex terrain to hydrodynamic roughness on a coral reef. *Journal of Physical Oceanography*, *748*(7), 1567–1587. https://doi.org/10.1175/jpo-d-18-0013.1

Rosman, J. H., & Hench, J. L. (2011). A framework for understanding drag parameterizations for coral reefs. *Journal of Geophysical Research*, *8116*(8), C08025. https://doi.org/10.1029/2010jc006892

Shaw, W. J., Trowbridge, J. H., & Williams, A. J. (2001). Budgets of turbulent kinetic energy and scalar variance in the continental shelf bottom boundary layer. *Journal of Geophysical Research*, *106*(C5), 9551–9564. https://doi.org/10.1029/2000jc000240

Takeshita, Y., McGillis, W., Briggs, E. M., Carter, A. L., Donham, E. M., Martz, T. R., & Smith, J. E. (2016). Assessment of net community production and calcification of a coral reef using a boundary layer approach. *Journal of Geophysical Research: Oceans*, *121*(8), 5655–5671. https://doi.org/10.1002/2016JC011886

Ullman, S. (1979). The interpretation of structure from motion. *Proceedings of the Royal Society of London. Series B. Biological Sciences*, *1203*(1153), 405–426. Retrieved from https://doi.org/10.1098/rspb.1979.0006